nature geoscience

ARTICLES

PUBLISHED ONLINE: 11 JANUARY 2016 | DOI: 10.1038/NGEO2623

Himalayan megathrust geometry and relation to topography revealed by the Gorkha earthquake

J. R. Elliott[1]*, R. Jolivet[2†], P. J. González[3], J.-P. Avouac[2,4], J. Hollingsworth[5], M. P. Searle[6] and V. L. Stevens[4]

The Himalayan mountain range has been the locus of some of the largest continental earthquakes, including the 2015 magnitude 7.8 Gorkha earthquake. Competing hypotheses suggest that Himalayan topography is sustained and plate convergence is accommodated either predominantly on the main plate boundary fault, or more broadly across multiple smaller thrust faults. Here we use geodetic measurements of surface displacement to show that the Gorkha earthquake ruptured the Main Himalayan Thrust fault. The earthquake generated about 1 m of uplift in the Kathmandu Basin, yet caused the high Himalaya farther north to subside by about 0.6 m. We use the geodetic data, combined with geologic, geomorphological and geophysical analyses, to constrain the geometry of the Main Himalayan Thrust in the Kathmandu area. Structural analyses together with interseismic and coseismic displacements are best explained by a steep, shallow thrust fault flattening at depth between 5 and 15 km and connecting to a mid-crustal, steeper thrust. We suggest that present-day convergence across the Himalaya is mostly accommodated by this fault—no significant motion on smaller thrust faults is required. Furthermore, given that the Gorkha earthquake caused the high Himalayan mountains to subside and that our fault geometry explains measured interseismic displacements, we propose that growth of Himalayan topography may largely occur during the ongoing post-seismic phase.

On 25 April 2015, a moment magnitude (M_w) 7.8 earthquake struck Nepal, rupturing beneath the higher parts of the Himalayas and resulting in more than 8,800 fatalities (Fig. 1). Initial seismological observations showed that the rupture initiated beneath the Gorkha region of central Nepal at 15 km depth, consistent with a low-angle thrust fault dipping at ~11° north. Finite fault rupture models from the United States Geological Survey (USGS) National Earthquake Information Center indicate that the rupture propagated eastward beneath Kathmandu for about 140 km. Early observations[1–4] suggest that the rupture did not reach the surface, contrasting with earlier events, such as the 1934 and 1255 M_w 8+ earthquakes in the same area[5] or the 2005 M_w 7.6 Kashmir earthquake at the western end of the Himalaya[6]. A pair of M_w 6.6–6.7 aftershocks occurred within the hour following the mainshock, at either end of the rupture (Fig. 1). An even larger aftershock (M_w 7.3) occurred at the northeastern end of the main rupture 17 days later, resulting in further fatalities.

The 2015 Gorkha earthquake occurred within a gap in historical seismicity[7,8] (Fig. 1). The most recent major earthquake in Nepal was the 1934 Nepal–Bihar earthquake with surface wave magnitude (M_s) ~ 8.2, which initiated 175 km east of Kathmandu[9] and propagated westward for approximately 150 km, causing severe shaking in eastern Nepal and the Ganga Plain[7]. Given its large magnitude, the location of its epicentre and the palaeo-seismological evidence for surface breaks[5], the 1934 event is likely to have ruptured the entire seismogenic thickness, from the aseismic shear zone to the surface. In the area of the Gorkha earthquake, a series of three large (magnitude, M, 7+) earthquakes occurred in 1833 (ref. 8), resulting in intense shaking around Kathmandu and to the south, but tapering off quickly to the north (Supplementary Fig. 1). Although reconstructing the spatial relationship between these different earthquakes is challenging, especially in the pre-instrumental period, it is clear that the 2015 earthquake ruptured only a small portion of the Main Himalayan Thrust (MHT), at the eastern edge of the 800-km-wide seismic gap between the 1905 M 7.8 Kangra earthquake in the west and the M 8.2 1934 earthquake in the east[10] (Fig. 1b). Given that the last event to have ruptured such a long portion of the megathrust was the 1505 M_w 8.2 earthquake[7,11], affecting western Nepal and northwest India, the intervening 500 years has resulted in the accumulation of a 10 m slip deficit along most of this stretch of the front[12].

The Gorkha earthquake provides an opportunity to investigate the role of seismic deformation in building the Himalaya: how the fault activated in this earthquake relates to the structure of the wedge and how the current topography of the range has developed. The Himalaya is an orogenic wedge formed by a stack of thrust sheets scraped off Indian crust as it was underthrust beneath the margin of Asia after closure of the Tethys Ocean[13]. All thrust faults within the wedge sole into a main basal décollement that coincides with a mid-crustal reflector at a depth of about 40 km beneath southern Tibet[14,15]. Debate is ongoing regarding how the wedge is deforming and the reason for the steep front of the high range lying about 100 km north from the southern end of the wedge (Fig. 1). Some authors have argued that the location of the front of the high topography could be explained by a mid-crustal ramp along the MHT (refs 16,17), or by a combination of ramp overthrusting and underplating associated with duplex development of the Himalayan wedge[18,19]. Conversely, others have

[1]COMET, Department of Earth Sciences, University of Oxford, Oxford OX1 3AN, UK. [2]COMET, Bullard Laboratories, Department of Earth Sciences, University of Cambridge, Cambridge CB3 OEZ, UK. [3]COMET, School of Earth & Environment, University of Leeds, Leeds LS2 9JT, UK. [4]Geological and Planetary Sciences, California Institute of Technology, Pasadena, California 91125, USA. [5]ARUP, 13 Fitzroy Street, London W1T 4BQ, UK. [6]Department of Earth Sciences, University of Oxford, Oxford OX1 3AN, UK. †Present address: Ecole Normale Supérieure, Department of Geosciences, PSL Research University, 75231 Paris, France. *e-mail: john.elliott@earth.ox.ac.uk

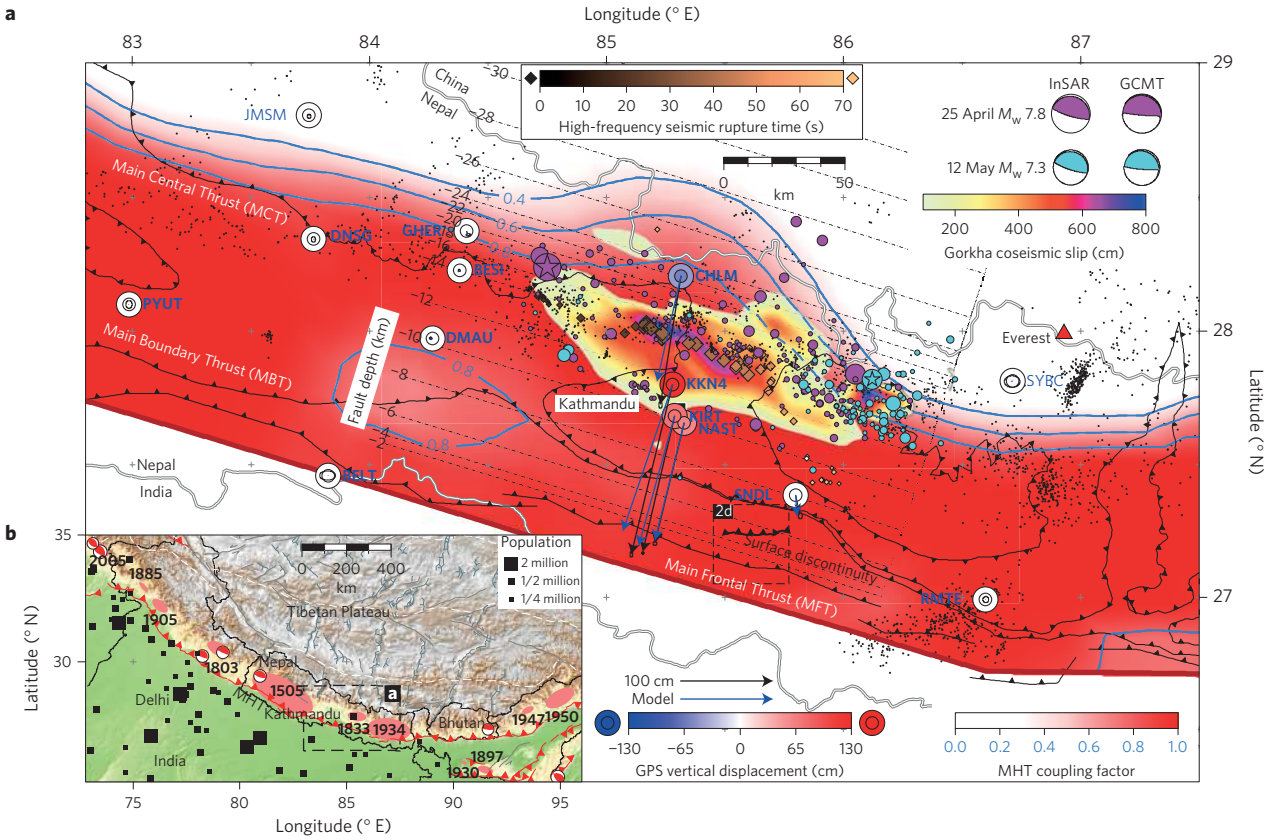

Figure 1 | Comparison of earthquake slip determined from surface geodetic displacements with long-term interseismic coupling. a, Coseismic slip distribution on the MHT (dashed depth contours) from the mainshock and largest aftershock (stars denote epicentres, circles aftershocks) and MHT coupling from interseismic deformation[25] (blue lines), and pre-earthquake background seismicity[12] (black dots). The spatio-temporal evolution of the high-frequency seismic sources during the earthquake rupture[1] follow the ramp-and-flat hinge line in our model at 14 km depth (copper diamonds). Black triangles indicate active Main Frontal Thrust trace[37] and Main Boundary and Central Thrusts. Blue-to-red coloured circles indicate measured (inner circle) and predicted (outer circle) vertical GPS coseismic displacements, and arrows indicate horizontal displacements (black, data; blue, model). **b**, Estimated extent of ruptures due to past large earthquakes[7,10] (pink ellipses). Magnitude 6+ reverse faulting earthquakes (1976–2015) are from the Global Centroid Moment Tensor (GCMT) catalogue[38].

argued for active out-of-sequence thrusting at the front of the high Himalaya[20,21].

Satellite observations of ground displacement

We combine radar and optical satellite images to measure ground displacements and determine the geometry and kinematics of thrust faulting for the Himalayas. We process Interferometric Synthetic Aperture Radar (InSAR) data from the European Space Agency (ESA) Sentinel-1 satellite to derive surface line-of-sight ground motion (Fig. 2 and Supplementary Fig. 2 and Supplementary Table 1) and surface offsets (Supplementary Fig. 3) from the correlation of amplitude images from both SAR and Landsat-8 (see Methods). We supplement these observations with other published surface displacements from the ALOS-2 SAR satellite[3], and GPS (Global Positioning System) coseismic offsets[2] (Supplementary Fig. 4). We observe up to 2 m of south-southwest motion and almost 1 m of uplift in the Kathmandu basin and the surrounding Lesser Himalaya, whereas north of this, a large region of the higher Himalaya subsided by about 0.6 m (Fig. 2).

The low gradient in the surface displacement field measured from both radar (Fig. 2 and Supplementary Fig. 2) and optical offset images (Supplementary Fig. 3) is consistent with slip during the 2015 Gorkha earthquake remaining buried at depth along the entire 150 km rupture length. None of the satellite geodetic measurements (that is, from InSAR, SAR azimuth correlation and optical image correlation) shows surface slip associated with the Main Frontal Thrust (MFT), which has important implications for interpreting seismological records. However, triggered near-surface slip is imaged with the Sentinel-1 coseismic interferograms (Fig. 2d and Supplementary Fig. 5) along a 26-km-long discontinuity, 10 km north of the MFT. This discontinuity in the interferometric phase follows the trace of the Main Dun Thrust (MDT), a relatively minor splay considered to be less active than the MFT (ref. 22). Independent interferograms on two overlapping descending tracks with acquisitions made 4 and 11 days after the mainshock show broadly consistent surface offsets, peaking with 6 cm of surface motion towards the radar. This surface displacement field at the fault trace is consistent with 12 cm of reverse slip, assuming a 30° northward-dipping plane[22], and happened during or shortly (that is, less than 4 days) after the mainshock. In the intervening 7 days before another SAR acquisition on a parallel track, fault slip along the central portion (5 km long) continued by a further ~2.5 cm motion along the radar line of sight (Fig. 2e), highlighting post-seismic slip on this secondary structure.

The geometry of the Main Himalayan Thrust

We seek to explore the range of possible geometries of the MHT explaining the surface displacement data of the mainshock (Fig. 3), accounting for what is known about the fault geometry at depth. From south to north, our fault model includes three segments to reflect the ramp–flat–ramp geometry: first, a shallow 30° north-dipping ramp between the surface and 5-km-depth, constrained

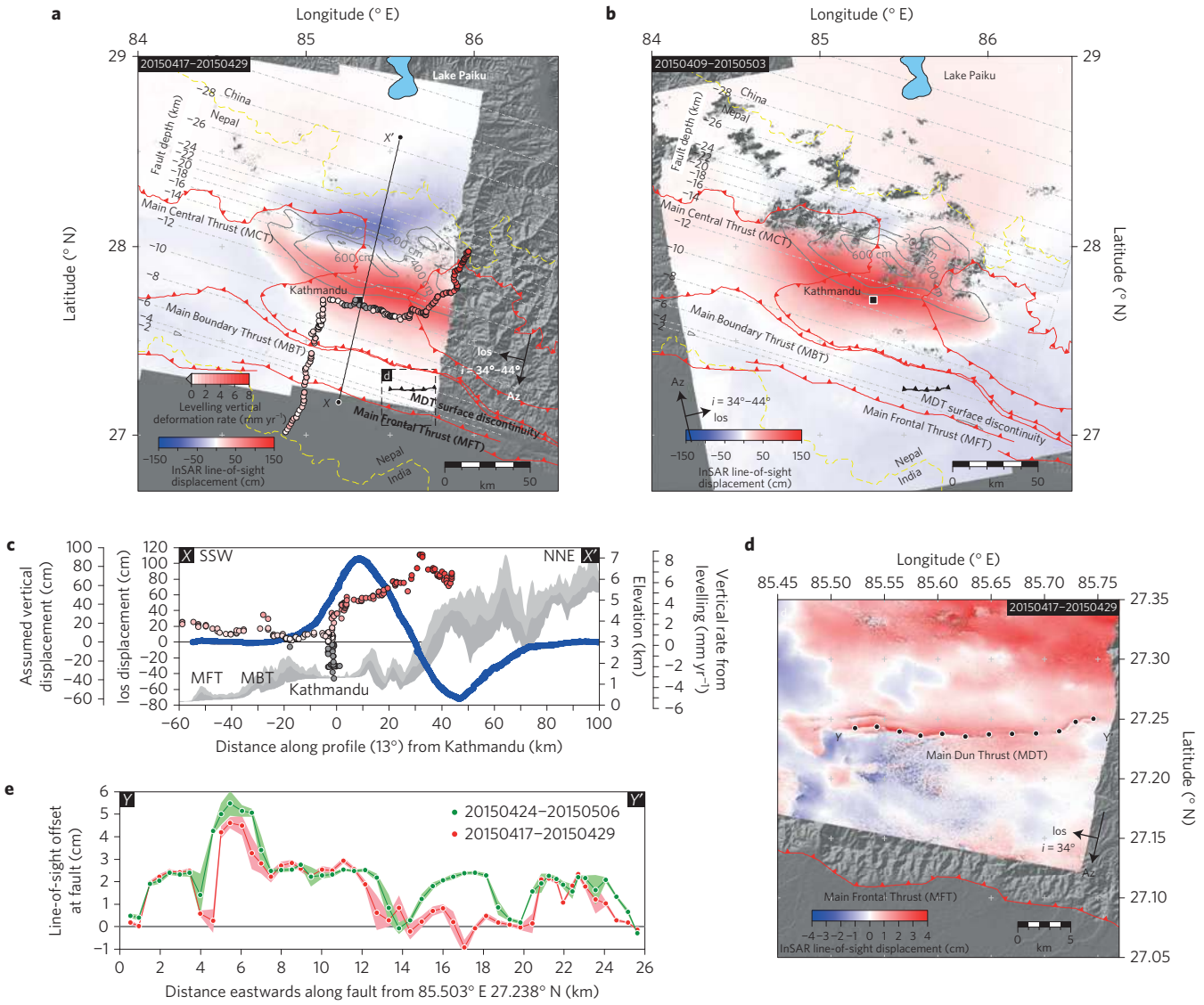

Figure 2 | Deformation patterns observed in Sentinel-1 interferograms for the 2015 Gorkha mainshock and comparison with long-term levelling data. **a**, Coseismic displacement field (positive towards satellite) with contour lines of modelled slip at depth, pre-earthquake interseismic vertical levelling rates[34] (coloured dots) and MFT surface trace[37]. Arrows indicates satellite azimuth (Az) and line-of-sight direction (los) with a vary angle of incidence angle (*i*). **b**, Coseismic ascending interferogram. **c**, North–south profile of the deformation (blue) in **a** compared with levelling uplift rates[34] (coloured circles—negative values denote localized non-tectonic subsidence around Kathmandu). **d**, Discontinuity in the displacement field in **a** along the Main Dun Thrust (MDT), consistent with ~12 cm of thrust motion on the MDT. Locations (black dots) of offsets given for every fourth point shown in **e**. **e**, Displacement offsets across the MDT are consistent from independent interferograms (**a**,**b**) suggesting slip happened during, or shortly after the Gorkha earthquake, with potential increase along the central section (14–19 km).

by structural sections in the area and approximately following the surface trace of the MFT (ref. 22) with a strike of N108°, second, a flat portion with a shallow angle reaching, finally, a steeper, mid-crustal, ramp. We systematically test a range of possible values of dip angles of the flat (1°–10°) and the mid-crustal ramp (1°–45°) together with possible horizontal distances for the hinge line defined by the top of the mid-crustal ramp and the MFT (50–120 km). For each case, we solve for the distribution of dip slip using a standard constrained least-squares approach and compute a weighted misfit for that solution (here the log-likelihood, see Methods and Supplementary Fig. 6). We consider that all geometric configurations giving a weighted misfit within 95% of the best configuration are acceptable models.

Within these bounds, the most likely dip angle for the flat portion of the MHT is constrained between 5° and 8° north. This geometry fits with the zone of high electrical conductivity imaged from magneto-telluric data[23] (Fig. 4), corresponding to wet sediments dragged along the MHT.

Further north, fault geometries consistent with surface geodetic data extend from models with no significant change in the dip angle (that is, no steep, mid-crustal, ramp) to models with a steep, mid-crustal, ramp. Although the peak distribution in changes of dip angle between the flat and the ramp segments for acceptable models is around a 5°–7° increase (Fig. 3), the geodetic data alone do not exclude the hypothesis of a flat MHT all the way into the Tibetan Plateau (Supplementary Fig. 7). However, additional data advocate for a steep, mid-crustal, structure north of the Kathmandu Basin. From interseismic GPS- and levelling-derived rates of motion, we use a Bayesian approach to infer the probability density function (PDF) of the location of the dislocation explaining elastic strain increase during the interseismic period (see Fig. 3, Methods and Supplementary Fig. 3). The tip of this aseismic shear

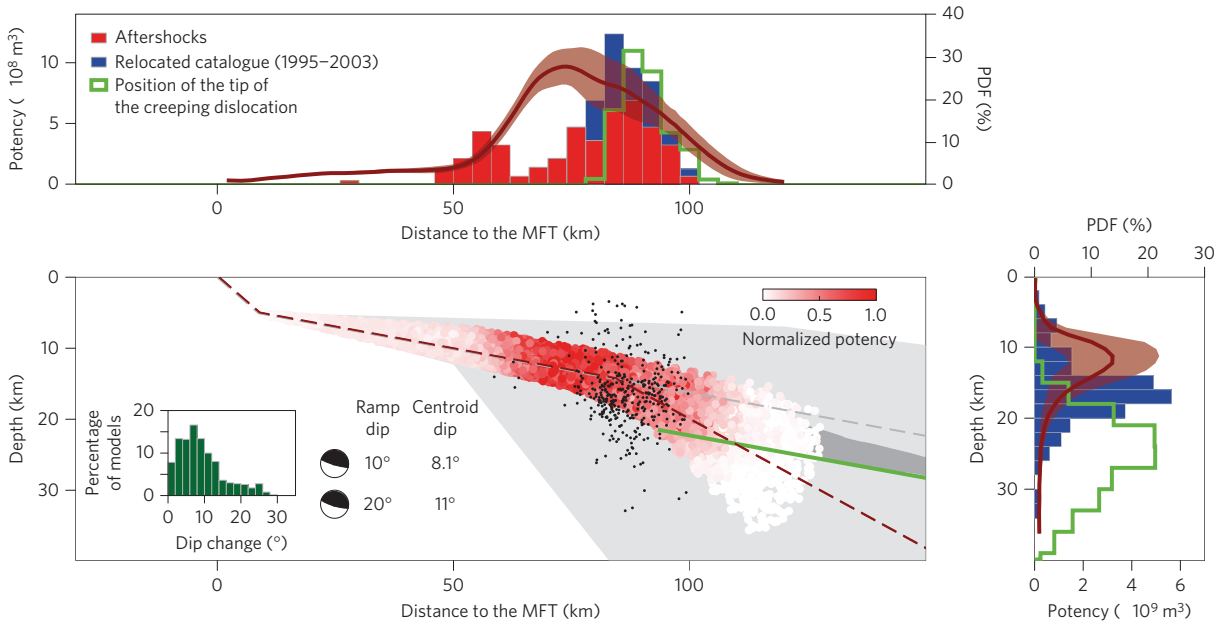

Figure 3 | MHT geometry exploration along a cross-section (N18°). White-to-red dots are slip potency from 500 models randomly picked inside the 95% best geometries out of the total range explored (grey). Dashed brown line is our proposed geometry. Grey dashed line is an alternative model without a kink. Green line is the creeping section of the MHT re-estimated in this study. Dark grey shading indicates the location of the main reflector in the InDepth[15] profile. Dark dots are micro-earthquakes before the Gorkha earthquake. Focal mechanisms are for two models with a 10° and 20° dip angle ramp. The dark green histogram shows the change in dip angle between flat and mid-crustal ramp for 500 acceptable models. Green histogram lines show the horizontal (top) and depth (right) location of the tip of the creeping section. Histograms show seismic activity before (1995–2003; blue) and after (red) the Gorkha earthquake. Dark red lines and shading show mean slip potency and standard deviation for 500 acceptable models.

zone (20–25 km, consistent with the location of the main reflector in the InDepth seismic reflection profile[15]) cannot be shallower than 15 km, but coseismic slip concentrates between 5 and 15 km depth, highlighting a clear depth separation between coseismic slip (5–15 km), the micro-seismic activity (15–20 km) and the aseismic shear zone (20–25 km). The same argument can be made for a similar separation in the direction perpendicular to the MHT (Fig. 3). Such offset requires a steep, mid-crustal, ramp connecting the flat seismogenic portion of the MHT to the deep, aseismic, shear zone.

Then, considering the case of a 15°–25° north-dipping mid-crustal ramp, the position of its shallow tip is constrained by surface coseismic displacements (80–90 km north of the MFT, Supplementary Fig. 6). This position of the hinge line between ramp and flat also fits with the location of the high-frequency sources (Figs 1 and 4) imaged by back-projection of teleseismic P waves[1]. This is consistent with a direct structural control on generating these seismic sources. By reconciling co- and interseismic geodetic surface displacements, micro-seismic activity and previous geologic interpretations of structure and river incisions, we propose the following detailed fault geometry of the MHT from south to north under the Kathmandu area (Fig. 4): first, a 30° north-dipping ramp from the surface (outcropping as the MFT) to 5 km depth followed by a 75-km-wide, 7°, north-dipping flat section that ends on a 20° north-dipping, 30-km-wide, mid-crustal ramp. This deeper ramp then intersects a shallow north-dipping shear zone of aseismic deformation, the latter coinciding well with the deeper portion of the MHT imaged seismically[15,24].

The maintenance of the steep front of the high Himalayan range probably owes itself to the mid-crustal ramp along the MHT. This transition zone also coincides with the down-dip edge of the locked zone (Fig. 1) as determined by measurements of interseismic strain[12,25]. Therefore, our proposed geometry of the MHT satisfies very well previous geophysical constraints, and is also consistent with geomorphic and geologic structural constraints for the Himalaya, allowing us to propose a unified cross-section across the range, from the Indian Plain in the south to the Tibetan Plateau in the north (Fig. 5). Of particular note, the ramp position is consistent with field observations of broadly folded foliations north of the Kathmandu Klippe thought to be related to duplex development in the Lesser Himalaya, as proposed along a number of geologic cross-sections across Nepal[26]. Our proposed fault geometry matches remarkably well the geometry of the MHT inferred from thermo-kinematic models adjusted to thermo-barometric and thermo-chronological data[19,27] or to one inferred from river incision[16]. Coseismic slip is constrained to the MHT at depth, with no out-of-sequence thrusting on the Main Central Thrust (MCT; Fig. 5). Within error, the present rate of interseismic shortening[25] matches the long-term slip rate on the MFT (ref. 22), excluding the possibility of substantial internal deformation of the wedge. Co- or early post-seismic near-surface slip on the MDT is the only detectable evidence of deformation off the MHT and corresponds to only ~10 cm of horizontal shortening, almost two orders of magnitude smaller than the deformation due to slip on the MHT. This is consistent with southward propagation of the thrust front through time from the MCT (active between 20 and 15 million years ago (Ma); ref. 28), Ramgarh thrust (active ~15–10 Ma), to the Main Boundary thrust (MBT, active from ~7–0 Ma), and eventually to the southernmost MFT (ref. 22; Fig. 5).

Constrained distribution of fault slip at depth

The slip distribution calculated for the proposed geometry shows peak slip of about 8 m, for a 140-km-long, 50–60-km-wide rupture (Figs 1 and 4), with more than 60% of the released moment located southward (that is up-dip) of the main cluster of pre-seismic micro-earthquakes and surrounded by aftershocks. Slip from the largest (M_w 7.3) aftershock that occurred 17 days later fills in most of the eastern gap in the slip contours at the lower down-dip edge of the fault rupture (Fig. 1 and Supplementary Fig. 12), where the aftershock activity was high early on. This major aftershock highlights a filling in of a gap in the mainshock slip in the east

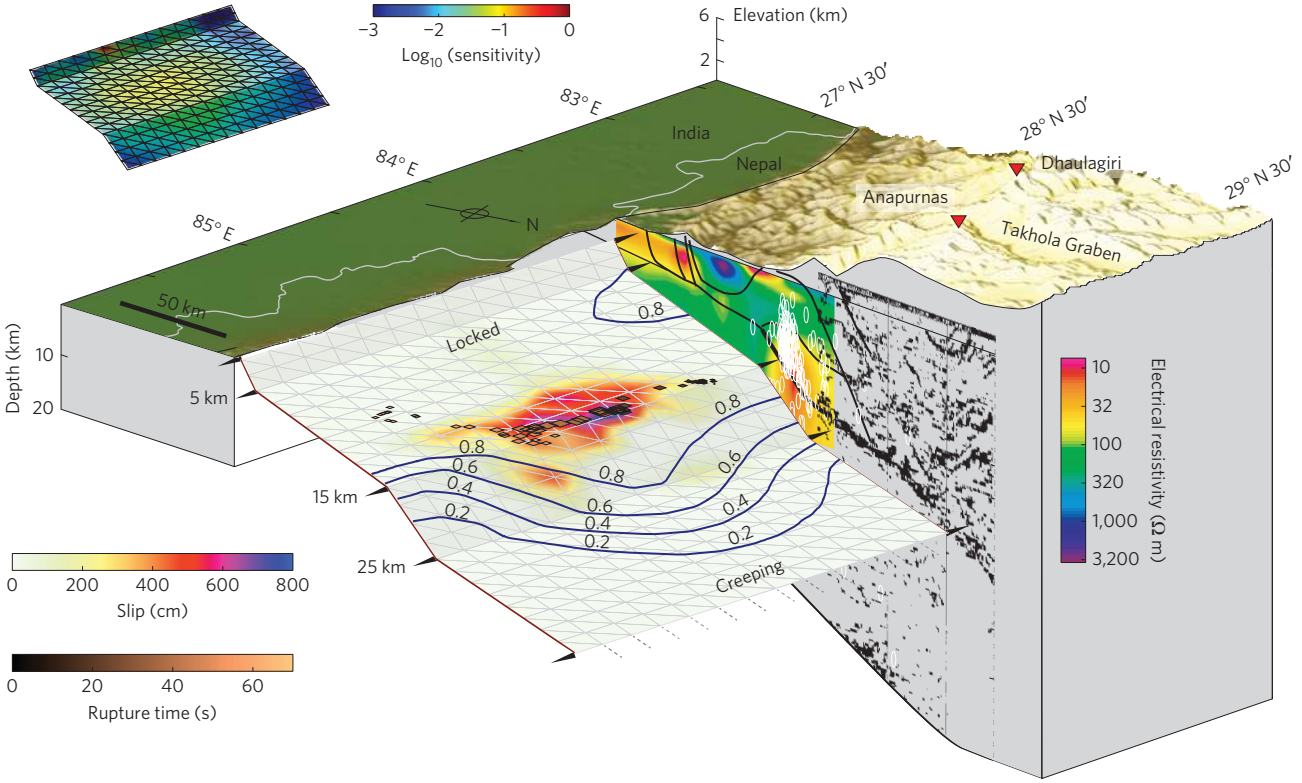

Figure 4 | Three-dimensional block diagram of the geometry proposed for the MHT. Colours denote earthquake slip relative to interseismic coupling (blue lines) inferred from GPS-, levelling- and InSAR-derived deformation rates before the Gorkha earthquake[25]. High-frequency seismic sources[1] during the earthquake rupture (diamonds), run along the ramp-and-flat hinge line at 14–15 km depth. The cross-section shows the InDepth reflection profile[14], the main faults (black lines) and an electromagneto-telluric image[23] highlighting the high conductivity (low resistivity) measured along the MHT. White ellipses are relocated micro-seismic activity before the Gorkha earthquake. Note the gap between the fault plane and cross-section for clarity. Inset: Model sensitivity *s* (defined as diag($\mathbf{G}'\mathbf{G}$) where $\mathbf{G}$ is the Green's function matrix) indicates the normalized sum of surface displacements caused by unit slip on each point on the fault.

after some delay, potentially caused by a rupture-impeding barrier of unknown origin (aseismic slip, geometrical complexity or low stress level).

Although most of the slip during the Gorkha earthquake occurred on the shallow flat portion of the MHT, slip tapers out on the mid-crustal ramp where interseismic creep is inferred to extend. This suggests either that the ramp slips in a mixture of seismic and aseismic behaviour, or that there is a broad zone of deformation over a 20 × 10 km region. However, no out-of-sequence thrusting in the high range is seen during the Gorkha earthquake, nor is it needed to explain the locally higher uplift and incision rates at the front of the high range given the location we find for the mid-crustal ramp. The northern limit of slip is contained within the locked zone (Fig. 1), which is consistent with the generic, globally observed, behaviour of active faults and megathrusts, in which seismic and aseismic portions seem mutually exclusive[29–31]. This would lead to a maximum possible rupture width of ∼100 km in this region[25]. At the shallow end of the rupture, slip tapers off over the relatively short distance of 5 km on the flat from greater than 3 m to less than 1 m at 11 km depth, no closer than 50 km from the MFT (Fig. 1). This abrupt up-dip limit of slip is markedly uniform along strike for the 140 km length rupture, and at a near constant depth of 11 km, where the sensitivity of our slip model is high. What controls the arrest of the rupture is not clear because this portion of the fault is locked during the pre-seismic period[12,25], and hence is anticipated to fail during an earthquake. Such a sharp up-dip limit on slip could result from other thrusts such as the MBT soleing out onto the MHT (Fig. 5). This would result in branch lines forming a structural complexity on the MHT interface, forming a wide damage zone that could impede the up-dip propagation of earthquake ruptures. This leaves a locked fault width that is at least as wide as that which ruptured in the 2015 earthquake (Fig. 4), but at a shallower depth. Similar constrained deeper slip leaving wide unruptured fault segments at shallower depths has been seen in smaller continental reverse earthquakes elsewhere[32]—in one case resulting in the continuation of seismic rupture after a one-year delay[33], the hiatus in that case most likely due to the interaction of the rupture plane with other intersecting fault segments at depth. Alternatively, a reduced stress level left from past earthquakes may also have limited the extent of the rupture. To the east, the 1934 Bihar–Nepal earthquake is thought to have ruptured the whole seismogenic depth, reaching the surface and reducing the stress level there. If this earthquake were to have propagated near the surface to the west (a possibility not excluded at present[5]), it would have also left a stress shadow up-dip of the Gorkha earthquake rupture. More accurate constraints on the extent of historic ruptures are key in addressing the role of stress shadowing along the MHT.

The growth of topography

The Himalaya rise over 5 km above the plains of India; their great height a result of crustal thickening due to the northward collision of India with Asia over millions of years. As a consequence of the Gorkha earthquake, however, the high range subsided by up to 60 cm (Supplementary Fig. 11), as a result of elastic extension north of the region of maximum southward slip as imaged in our model (Figs 2c and 5). As the rest of the locked portion of the MHT, prone to rupture in earthquakes, is located even farther southward from the main slip zone found here, we can assume that

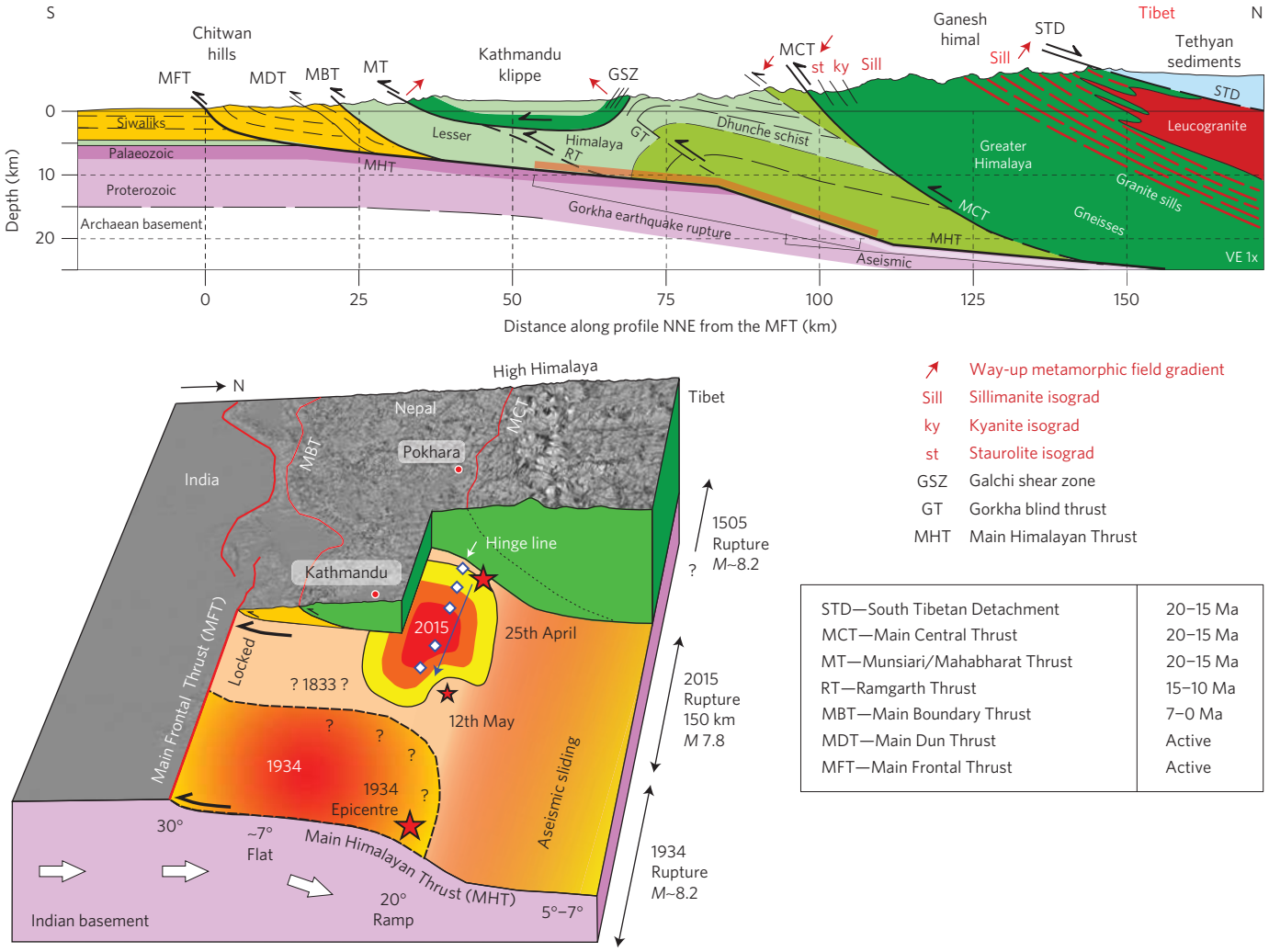

STD—South Tibetan Detachment	20–15 Ma
MCT—Main Central Thrust	20–15 Ma
MT—Munsiari/Mahabharat Thrust	20–15 Ma
RT—Ramgarth Thrust	15–10 Ma
MBT—Main Boundary Thrust	7–0 Ma
MDT—Main Dun Thrust	Active
MFT—Main Frontal Thrust	Active

Figure 5 | Geologic cross-section incorporating the Main Himalayan Thrust geometry, and schematic cartoon of the 2015 rupture area relative to previous earthquakes. Top: Geologic north–south profile across the Ganesh–Langtang Himalaya with periods of activity of the major Himalaya Thrusts denoted. Bottom: Location of the 2015 earthquake and its aftershock on the resolved MHT geometry (with the upper plate removed to reveal the slip zone). High-frequency seismic sources[1] are marked as diamonds running along the hinge line between the ramp and flat. The M_w 7.2 aftershock occurred at the eastern end of the main rupture. The rupture extents of previous earthquakes from 1934 ($M \sim 8.2$), 1833 ($M \sim 7.6$) and 1505 ($M \sim 8.2$) are poorly constrained. VE, vertical exaggeration.

all major thrusting seismic events in the region will tend to lower the high Himalayan topography. However, on average, over multiple earthquake cycles, the long-term uplift of the high Himalaya is about 4 mm yr^{-1} (ref. 19).

The peak uplift rate in the high Himalaya relative to the Gangetic Plain measured from levelling[34] and InSAR (ref. 35) over recent decadal timescales is about 7 mm yr^{-1}, larger than the 4 mm yr^{-1} long-term uplift for the high Himalaya[19]. The difference might be due to coseismic subsidence observed during the Gorkha earthquake (up to 60 cm) and expected from future earthquakes (the locked portion of the MHT lies south of the high chain). We therefore conclude that long-term uplift of the high chain occurs primarily in the time period between large earthquakes on the MHT. Current geodetic shortening rates[12,25] agree with longer-term slip rates on the MHT. Furthermore, assuming our preferred fault geometry is correct, the contribution of elastic deformation to uplift predicted from the projection of the regional distribution of coupling on our geometry[25] matches with the uplift rates in the interseismic period[34] (Supplementary Fig. 9). Therefore, only a small fraction of the interseismic strain translates into permanent deformation. Consequently, the 3–4 mm yr^{-1} long-term uplift at the front of the high chain must primarily result from ramp overthrusting during transient episodes of deformation. Post-seismic slip could be an efficient way of building topography at the front of the chain and the next few years of observations will allow one to verify this hypothesis.

We have reconciled a suite of independent observations of Himalayan faulting and derived a proposed geometry of the MHT satisfying geologic, geophysical and geomorphic constraints gathered from numerous studies. This understanding of the fault geometry may now be used as a basis for further investigation on the seismogenic behaviour of the Himalayan front in the region of Kathmandu, as well as a starting point for long-term models for building of the highest mountain range in the world. Our results also highlight the potential for structural control on the propagation and arrest of earthquake rupture fronts: that is, in the generation of high-frequency seismic waves along the hinge line defining the ramp–flat transition; and the possible arrest of up-dip rupture from branching faults soleing into the MHT. The latter finding highlights a large, shallow region of the MHT south of Kathmandu that has not ruptured in this event, but is locked, and therefore still has the potential to fail seismically.

Methods

Methods and any associated references are available in the online version of the paper.

Received 30 June 2015; accepted 26 November 2015; published online 11 January 2016

References

1. Avouac, J.-P., Meng, L., Wei, S., Wang, T. & Ampuero, J.-P. Lower edge of locked Main Himalayan Thrust unzipped by the 2015 Gorkha earthquake. *Nature Geosci.* **8,** 708–711 (2015).
2. Galetzka, J. *et al.* Slip pulse and resonance of the Kathmandu basin during the 2015 Gorkha earthquake, Nepal. *Science* **349,** 1091–1095 (2015).
3. Lindsey, E. *et al.* Line of sight displacement from ALOS-2 interferometry: M_w 7.8 Gorkha Earthquake and M_w 7.3 aftershock. *Geophys. Res. Lett.* **42,** 6655–6661 (2015).
4. Wang, K. & Fialko, Y. Slip model of the 2015 M_w 7.8 Gorkha (Nepal) earthquake from inversions of ALOS-2 and GPS data. *Geophys. Res. Lett.* **42,** 7452–7458 (2015).
5. Sapkota, S. N. *et al.* Primary surface ruptures of the great Himalayan earthquakes in 1934 and 1255. *Nature Geosci.* **6,** 71–76 (2013).
6. Avouac, J.-P., Ayoub, F., Leprince, S., Konca, O. & Helmberger, D. V. The 2005, M_w 7.6 Kashmir earthquake: sub-pixel correlation of ASTER images and seismic waveforms analysis. *Earth Planet. Sci. Lett.* **249,** 514–528 (2006).
7. Ambraseys, N. N. & Douglas, J. Magnitude calibration of north Indian earthquakes. *Geophys. J. Int.* **159,** 165–206 (2004).
8. Bilham, R. Earthquakes in India and the Himalaya: tectonics, geodesy and history. *Annu. Geophys.* **47,** 839–858 (2004).
9. Chen, W.-P. & Molnar, P. Seismic moments of major earthquakes and the average rate of slip in central Asia. *J. Geophys. Res.* **82,** 2945–2970 (1977).
10. Bilham, R., Gaur, V. K. & Molnar, P. EARTHQUAKES: Himalayan seismic hazard. *Science* **293,** 1442–1444 (2001).
11. Ambraseys, N. & Jackson, D. A note on early earthquakes in northern India and southern Tibet. *Curr. Sci.* **84,** 570–582 (2003).
12. Ader, T. *et al.* Convergence rate across the Nepal Himalaya and interseismic coupling on the Main Himalayan Thrust: implications for seismic hazard. *J. Geophys. Res.* **117,** B04403 (2012).
13. Searle, M. P. *et al.* The closing of Tethys and the tectonics of the Himalaya. *Geol. Soc. Am. Bull.* **98,** 678–701 (1987).
14. Hauck, M. L., Nelson, K. D., Brown, L. D., Zhao, W. & Ross, A. R. Crustal structure of the Himalayan orogen at 90 east longitude from Project INDEPTH deep reflection profiles. *Tectonics* **17,** 481–500 (1998).
15. Nábělek, J. *et al.* Underplating in the Himalaya-Tibet collision zone revealed by the Hi-CLIMB experiment. *Science* **325,** 1371–1374 (2009).
16. Lavé, J. & Avouac, J. P. Fluvial incision and tectonic uplift across the Himalayas of central Nepal. *J. Geophys. Res.* **106,** 26561–26591 (2001).
17. Pandey, M. R., Tandukar, R. P., Avouac, J. P., Lave, J. & Massot, J. P. Interseismic strain accumulation on the Himalayan Crustal Ramp (Nepal). *Geophys. Res. Lett.* **22,** 751–754 (1995).
18. Bollinger, L. *et al.* Thermal structure and exhumation history of the Lesser Himalaya in central Nepal. *Tectonics* **23,** TC5015 (2004).
19. Herman, F. *et al.* Exhumation, crustal deformation, and thermal structure of the Nepal Himalaya derived from the inversion of thermochronological and thermobarometric data and modeling of the topography. *J. Geophys. Res.* **115,** BO6407 (2010).
20. Wobus, C., Heimsath, A., Whipple, K. & Hodges, K. Active out-of-sequence thrust faulting in the central Nepalese Himalaya. *Nature* **434,** 1008–1011 (2005).
21. Wobus, C. W., Hodges, K. V. & Whipple, K. X. Has focused denudation sustained active thrusting at the Himalayan topographic front? *Geology* **31,** 861–864 (2003).
22. Lavé, J. & Avouac, J. P. Active folding of fluvial terraces across the Siwaliks Hills, Himalayas of central Nepal. *J. Geophys. Res.* **105,** 5735–5770 (2000).
23. Lemonnier, C. *et al.* Electrical structure of the Himalaya of central Nepal: high conductivity around the mid-crustal ramp along the MHT. *Geophys. Res. Lett.* **26,** 3261–3264 (1999).
24. Nelson, K. D. *et al.* Partially molten middle crust beneath Southern Tibet: synthesis of Project INDEPTH results. *Science* **274,** 1684–1688 (1996).
25. Stevens, V. & Avouac, J.-P. Coupling on the Main Himalayan Thrust. *Geophys. Res. Lett.* **42,** 5828–5837 (2015).
26. Robinson, D. M. *et al.* Kinematic model for the Main Central thrust in Nepal. *Geology* **31,** 359–362 (2003).
27. Bollinger, L., Henry, P. & Avouac, J. P. Mountain building in the Nepal Himalaya: thermal and kinematic model. *Earth Planet. Sci. Lett.* **244,** 58–71 (2006).
28. Kohn, M. J., Wieland, M. S., Parkinson, C. D. & Upreti, B. N. Miocene faulting at plate tectonic velocity in the Himalaya of central Nepal. *Earth Planet. Sci. Lett.* **228,** 299–310 (2004).
29. Chlieh, M., Avouac, J. P., Sieh, K., Natawidjaja, D. H. & Galetzka, J. Heterogeneous coupling of the Sumatran megathrust constrained by geodetic and paleogeodetic measurements. *J. Geophys. Res.* **113,** B05305 (2008).
30. Loveless, J. P. & Meade, B. J. Spatial correlation of interseismic coupling and coseismic rupture extent of the 2011 $M_W = 9.0$ Tohoku-oki earthquake. *J. Geophys. Res.* **38,** L17306 (2011).
31. Jolivet, R., Simons, M., Agram, P. S., Duputel, Z. & Shen, Z.-K. Aseismic slip and seismogenic coupling along the central San Andreas Fault. *Geophys. Res. Lett.* **42,** 297–306 (2015).
32. Elliott, J. R., Copley, A. C., Holley, R., Scharer, K. & Parsons, B. The 2011 M_w 7.1 Van (Eastern Turkey) earthquake. *J. Geophys. Res.* **118,** 1619–1637 (2013).
33. Elliott, J. R. *et al.* Depth segmentation of the seismogenic continental crust: the 2008 and 2009 Qaidam earthquakes. *Geophys. Res. Lett.* **38,** L06305 (2011).
34. Jackson, M. & Bilham, R. Constraints on Himalayan deformation inferred from vertical velocity fields in Nepal and Tibet. *J. Geophys. Res.* **99,** 13897–13912 (1994).
35. Grandin, R. *et al.* Long-term growth of the Himalaya inferred from interseismic InSAR measurement. *Geology* **40,** 1059–1062 (2012).
36. Wessel, P. & Smith, W. H. F. New, improved version of generic mapping tools released. *EOS Trans. AGU* **79,** 579 (1998).
37. Taylor, M. & Yin, A. Active structures of the Himalayan-Tibetan orogen and their relationships to earthquake distribution, contemporary strain field, and Cenozoic volcanism. *Geosphere* **5,** 199–214 (2009).
38. Ekström, G., Nettles, M. & Dziewo ski, A. M. The global CMT project 2004–2010: centroid-moment tensors for 13,017 earthquakes. *Phys. Earth Planet. Inter.* **200,** 1–9 (2012).

Acknowledgements

This work was supported by the UK Natural Environmental Research Council (NERC) through the Looking Inside the Continents (LiCS) project (NE/K011006/1), the Earthquake without Frontiers (EwF) project (EwF_NE/J02001X/1_1), and the Centre for the Observation and Modelling of Earthquakes, Volcanoes and Tectonics (COMET, GA/13/M/031, http://comet.nerc.ac.uk). The Sentinel-1A interferograms presented are a derived work of Copernicus data, subject to the ESA use and distribution conditions. R.J. is supported by the Marie Curie FP7 Initial Training Network iTECC (investigating Tectonic Erosion Climate Couplings). We are grateful to E. Lindsey and colleagues for making ALOS-2 displacements available at http://topex.ucsd.edu/nepal. We thank A. Copley, S. K. Ebmeier, P. England, A. Hooper, J. Jackson, B. Parsons, R. Walters and T. Wright for discussions. Most figures were made using the public domain Generic Mapping Tools[36].

Author contributions

The first two authors each contributed equally to the study. J.R.E. wrote the manuscript and processed Sentinel offset data. R.J. performed the fault modelling. P.J.G. processed the Sentinel interferograms. J.-P.A. conceived the research idea. J.H. processed the optical offset data. M.P.S. constructed the geologic cross-section. V.L.S. produced the interseismic coupling map. All authors took part in finalizing the manuscript.

Additional information

Supplementary information is available in the online version of the paper. Reprints and permissions information is available online at www.nature.com/reprints. Correspondence and requests for materials should be addressed to J.R.E.

Competing financial interests

The authors declare no competing financial interests.

Methods

Sentinel-1 InSAR. We use data acquired by the European Space Agency's (ESA's) Sentinel-1A, a synthetic aperture radar (SAR) satellite with a C-band radar frequency at 5.4050005 GHz (wavelength ~5.545 cm). We use single-look complex (SLC) data to compute differential interferograms (InSAR) of ground motion using the commercial GAMMA software package (http://www.gamma-rs.ch). Both the original SLC data and the interferograms (and associated metadata) we calculate to use in this study are archived and available to download from the Centre for Environmental Data Archival at http://www.ceda.ac.uk.

We form 12- and 24-day interferograms covering both the mainshock on 25 April and the largest aftershock on 12 May (Supplementary Table 1). Tight orbital control by ESA with frequent satellite manoeuvres has resulted in relatively narrow orbital tubes being maintained, yielding small perpendicular baselines of less than ~150 m. This greatly reduces geometric decorrelation and residual topographic effects in this region of very steep relief. Sentinel-1 implements a new acquisition mode, Terrain Observation by Progressive Scans (TOPS). Each TOPS radar image is composed of multiple along-track (azimuth) bursts, or subimages (typically 9–10 per scene, total length ~180 km), which overlap slightly to ensure data continuity (this is in addition to the SLC data scene comprising three subswaths in range, each 78–86 km wide). The full-resolution SLC images have a pixel size of 2.3 m in range and 14 m in azimuth, resulting in about 68,000 samples in range and 13,000 in azimuth per scene. The local angle of incidence ranges from 33° in the near range to 44° in the far range.

The bursts in TOPS mode are the result of an azimuth scanning acquisition, which induces a strong azimuth variable Doppler. To obtain successful differential interferograms with this new radar system, an improved co-registration method needs to be applied. This precise co-registration procedure minimizes the phase dependence of the azimuth variable Doppler. We used a TOPS co-registration method based on the geometric approach[39]. Precise orbits are first used to resample the slave image onto the master geometry, and then subsequently a refinement is made using a constant offset in range and azimuth between master and slave that is estimated using a number of patches across the images. The estimation of this offset and subsequent resampling of the slave radar SLC is iterated with a cross-correlation method until the estimated change in offset converges on less than 0.02 of an azimuth pixel. Jumps in phase at burst overlap regions in computed interferograms can still exist even after this level of precision in the co-registration, resulting in sharp discontinuities. Therefore, finally, a very precise offset in azimuth is estimated using the double-difference phases between bursts using the overlap regions (spectral diversity method), taking advantage of the strong Doppler variation within each burst. The phase offset relates linearly to the azimuth co-registration error, but this also relies on the overlap region between bursts being coherent. Once a very precisely co-registered slave image is obtained, this can then be further processed with the master using a two-pass interferometric method, using the 1-arcsec Shuttle Radar Topography Mission (SRTM) Digital Elevation Model to remove the contribution from topography. The resulting differential phase was spectrally filtered with an iterative method[40], and unwrapped using a minimum cost flow algorithm, before geocoding at ~100 m spacing.

The InSAR data reveal a predominately long-wavelength signal indicative of buried slip, and no discontinuities in phase associated with slip on the MFT are seen. However, surface slip was imaged in the Sentinel-1 interferograms covering the Main Dun Thrust (Supplementary Fig. 5), as seen in an east–west discontinuity in phase that runs for over 26 km. The magnitude of offset across this fault also seems to increase along part of its length in the post-seismic period between Sentinel-1 acquisitions on overlapping tracks.

We also calculate the surface offsets from correlating radar amplitudes. After first co-registering the master and slave full-resolution SLCs as described before, we estimate the offsets in both range and azimuth using a search window of 128 pixels and stepping 2 pixels in each direction. The offsets are calculated on the basis of the spatial correlation function within the window area from the cross-correlation of the image intensity, and the method relies on amplitude contrast within the estimation window. The offsets are then converted into displacements in range and azimuth, geocoded and then median filtered with a width of 2 km for range estimates and 10 km for azimuth. Given that the earthquake displacements are of the order or smaller than the pixel size, the signals retrieved by the cross-correlation method are relatively noisy. Additionally, the data coverage from the interferometric phase data is good owing to the high coherence, so the range offsets are not used to constrain the inversion. Furthermore, as the azimuth pixel size is large (14 m), offsets in this direction are too noisy to constrain the inversion, but are shown as a comparison with the offsets predicted from the modelling as a distinctive signal is apparent (Supplementary Fig. 3).

Optical offsets. We use optical image correlation to determine the coseismic horizontal displacement field resulting from the Gorkha earthquake. This technique measures the displacement of pixels between pre- and post-earthquake satellite images. First, using a sliding window, we measure the local frequency content at the same location in both pre- and post-earthquake images. Horizontal displacements (north–south and east–west component) are then determined from the phase shift of the low-frequency content between the two images within each sliding window location. Using this phase correlation method, we are able to resolve sub-pixel displacements of less than 1/15 of the Landsat8 pixel resolution (that is <1 m). This whole process is completed using the COSI-Corr software package[41–44], which is available for free download from www.tectonics.caltech.edu/slip_history/spot_coseis/index.html. Further details can be found in the Supplementary Information.

Fault geometry and slip modelling. The fault modelling and geometry was performed using the software code Classic Slip Inversion, which will be released soon and in the interim can be requested from R.J. The calculation of Green's functions in a layered elastic half-space was achieved using the EDKS software[45].

Fault geometry of the MHT. We fix the shallow geometry to the structure previously described in cross-sections[16]. A shallow ramp with a N108° strike extends from the surface to a depth of 5 km with a 30° dip angle. Below this, a flat section with a shallow dip angle extends until the fault steepens to build a deeper ramp with a steeper dip angle. Geologic and geomorphological reconstructions constrain a dip angle of about 5°–7° for the flat portion of the Main Himalayan Thrust (MHT). The location of the tip of the creeping dislocation required to explain the interseismic displacements[35] is at about 90 km north of the Main Frontal Thrust (MFT) and about 25 km deep. Our own estimates suggest comparable values. Therefore, to join the mid-crustal flat portion and the deep shear zone, we need to introduce a steep, mid-crustal ramp. However, the position of that steeper ramp with respect to the MFT is loosely constrained. We test a wide range of values for the dip angle of the flat portion of the MHT (that is, from 1° to 10°), the position of the top of the deep ramp (that is, from 50 to 100 km north of the MFT) and its dip angle (that is, from 1° to 40°).

InSAR data downsampling. We downsample the InSAR data using a quad tree algorithm based on the curvature of the displacement field[46]. Each interferogram is downsampled using a 20-km-wide squared window. We then iteratively split each window into 4 equally sized windows until the curvature of the resulting displacement field is smaller than a threshold value (here, 0.3 cm km^2 for the Sentinel-1 interferograms and 0.6 cm km^2 for the ALOS-2 interferograms), yielding 360, 476 and 433 data points for interferograms on Sentinel tracks 19, 85 and 121, and 582 and 262 data points for interferograms on ALOS-2 tracks 48 and 157, respectively. See Supplementary Fig. 10 to evaluate the effect of the downsampling.

InSAR data empirical covariance estimation. We estimate for each interferogram the empirical covariance function describing covariances as a function of distance between pixels[47,48]. We randomly pick a large set (~20,000) of pixels in a region where no deformation is observed and compute the empirical covariance function, $\mathrm{Cov}(x)$, written:

$$\mathrm{Cov}(x) = \frac{1}{2N(x)} \sum_{|i,j|_2 = x} (\phi_i, \phi_j) \quad (1)$$

where x is the distance between pixels, $N(x)$ is the number of pixels separated by a distance x, and ϕ_i and ϕ_j are the line-of-sight displacement of pixels i and j, respectively. We fit this empirical covariance function using an exponential decay for each interferogram independently as a function of distance writing:

$$\mathrm{Cov}(x) = \sigma^2 \mathrm{e}^{-x/\lambda} \quad (2)$$

where σ, the auto-covariance (that is, covariance for 0-distance), and λ, the characteristic length of the noise distribution, are the two estimated parameters. We use the resulting parameters to build the data covariance matrix, $\mathbf{C}_\mathrm{d}$, used in the slip inversion procedure (Supplementary Fig. 10).

Inverting for the distribution of slip given a fault geometry. Given a fault geometry, we solve for the distribution of slip that best fits our data. We discretize our fault geometry into 40, 60 and 80 km^2 triangles on the shallow ramp, mid-crustal flat and mid-crustal ramp respectively. Slip on the fault is the linear interpolation of the values on each node of the discretized mesh. Green's functions, $\mathbf{G}$ (that is, surface displacements for unit slip on each node), are computed assuming a layered elastic half-space with a previously used velocity structure[17] using the EDKS software[45].

Then, for a given set of geodetic data, $\mathbf{d}$, we find the model $\mathbf{m}$ using a constrained least-squares approach that minimizes the cost function $S(\mathbf{m})$ defined as:

$$\mathrm{S}(\mathbf{m}) = \frac{1}{2}((\mathbf{m}-\mathbf{m}_0)\mathbf{C}_m^{-1}(\mathbf{m}-\mathbf{m}_0) + (\mathbf{d}-\mathbf{G}\mathbf{m})\mathbf{C}_\mathrm{d}^{-1}(\mathbf{d}-\mathbf{G}\mathbf{m})) \quad (3)$$

where $\mathbf{m}$ is the vector of dip slip, constrained to be positive, $\mathbf{m}_0$ is the prior model (that is, here set to zero because our a priori is that the fault does not slip), $\mathbf{G}$ is the

Green's functions matrix (hence, **Gm** is the model prediction). We assume that slip in the direction along the fault strike is negligible. $\mathbf{C}_d$ is the data covariance matrix that is built under the assumptions that the data sets are independent from one another, the InSAR covariances can be derived from the noise structure determined empirically, and the GPS coseismic displacements are independent from one another. $\mathbf{C}_m$ is the model covariance matrix used here to regularize the inverse problem, written as,

$$\mathbf{C}_m = \gamma \nabla_s' \nabla_s \quad (4)$$

where γ is a hyper-parameter chosen on the basis of compromise between misfit and roughness of the solution and ∇_s is the Laplacian operator ∇, weighted by the model sensitivity defined as $s = \mathrm{diag}(\mathbf{G}'\mathbf{G})$. Such modulation allows for smoother (respectively, rougher) distribution of slip where the model has a low (respectively, high) sensitivity[49].

We provide the final distribution of slip of our best model, with our preferred geometry as Supplementary files at each node of our triangulated fault mesh (Supplementary Data 1), and the linear interpolation of slip on small triangles (Supplementary Data 2).

Inversion strategy to explore the geometry of the MHT. We explore a wide range of dip angles of the flat portion, α (Supplementary Fig. 6), and of the ramp of the MHT, β, together with the distance between the top of the ramp and the MFT, X. We test values of the dip angle of the flat α between 1° and 10°. We test values of the dip angle of the ramp β between 1° and 40°. We test values of the top of the ramp X between 50 and 100 km. We do not evaluate cases of a ramp shallower than the flat portion of the MHT.

Using a grid search approach (that is, testing all of the cases), for each triplet of value, we build the corresponding fault geometry, compute the corresponding Green's function, solve the least-squares problem and compute the logarithm of the posterior likelihood, $\mathrm{P}(\mathbf{m}|\mathbf{d})$, defined as:

$$\log(\mathrm{P}(\mathbf{m}|\mathbf{d})) = -\frac{1}{2}(\mathbf{d}-\mathbf{Gm})'\mathbf{C}_d^{-1}(\mathbf{d}-\mathbf{Gm}) \quad (5)$$

where **d** is the vector of surface displacements from InSAR and GPS data, **G** is the Green's function matrix, **m** is the vector of slip along the fault and $\mathbf{C}_d$ is the data covariance matrix. This formula is effectively the log-likelihood in Bayes' theorem and is used here as a weighted misfit function.

In Supplementary Fig. 6, we show the log-likelihood, normalized between the best and worst values we obtained, for different values of dip angle of the flat portion of the MHT, α, as a function of the distance between the MFT and the top of the ramp, X, and of the dip angle of the mid-crustal ramp, β. We consider that models with a log-likelihood within 95% of the best model are acceptable. This range of models is represented by the grey dashed contour in Supplementary Fig. 6. The best models suggest that the dip angle of the flat portion of the megathrust, α, is of about 4°–9°. We randomly pick 500 models among these 95% best models (black dots in Supplementary Fig. 6) to represent where slip potency is released during the 2015 Gorkha earthquake and to compute a histogram of change in dip angle (see Fig. 3 of the main text), suggesting that most acceptable models show a variation in dip angle of the order of 3°–10°.

Locating a deep creeping dislocation to explain interseismic displacement rates. Interseismic displacement rates in the Himalaya collision zone can be explained by a creeping dislocation dipping 5°–10° north, embedded at depth in a layered elastic half-space[12,35] with a previously used velocity structure[17] as implemented in the coseismic modelling here, using the EDKS software[45]. We propose here to locate this dislocation (shown as a green line in Fig. 3 of the main text) using a Bayesian approach to first test previous results[35], then derive a model consistent in terms of geometry with our study (in terms of projection along a N18° profile, mostly) and finally derive uncertainties from geodetic data. We use the GPS-[12] and levelling-derived[34] displacement rates (Supplementary Fig. 8). We solve for the depth, D, of the tip of the dislocation, for its dip angle, δ, for the distance to the MFT, X_{deep}, and for the rate of dip slip, $\dot{s}$ (see Supplementary Fig. 6). We use a Metropolis–Hastings algorithm implemented in the Pymc library[50] to sample the posterior PDF of the models, $\mathrm{P}(\mathbf{m}|\mathbf{d})$ defined by Bayes' theorem as

$$\mathrm{P}(\mathbf{m}|\mathbf{d}) = \mathrm{P}(\mathbf{m})\mathrm{e}^{-1/2(\mathbf{d}-\mathscr{G}(\mathbf{m}))'\mathbf{C}_d^{-1}(\mathbf{d}-\mathscr{G}(\mathbf{m}))} \quad (6)$$

where **d** is the geodetic-derived displacement rates (horizontal and vertical) over the interseismic period, **m** is the model parameters, $\mathrm{P}(\mathbf{m})$ is the prior PDF of the model (that is, what we know before the input from any data), $\mathscr{G}(\mathbf{m})$ is the prediction from the model and $\mathbf{C}_d$ is the data covariance matrix. $\mathrm{P}(\mathbf{m})$ is a uniform distribution between 70 and 120 km for X_{deep}, between 0 and 40 km for D, between 2° and 10° for δ and between 0 and 4 cm yr^{-1} for $\dot{s}$. $\mathbf{C}_d$ is a diagonal matrix with uncertainties derived from previous studies[12,34] on the diagonal. Our Monte Carlo chain has 10^4 samples leaving out the first 5×10^3 as a burning phase.

Analysis of the posterior PDFs (Supplementary Fig. 8) suggests that the distance between the MFT and the tip of the interseismic creeping dislocation is about 85–90 km, at a depth of 20–25 km, for a 1.8–2.0 cm yr^{-1} slip rate. The dip angle of the dislocation is not constrained, because of a lack of data over the Tibetan Plateau. These results are consistent with a previous study[35] and confirm the need for a mid-crustal, steep, ramp that would connect the upper, 7°, north-dipping flat that ruptured during the Gorkha earthquake and the interseismic shear zone at depth.

Mainshock results. The fits to the data based on the slip model for the mainshock are shown in Supplementary Fig. 2 for the full-resolution InSAR, and in Supplementary Fig. 4 for the GPS. Comparison of model predictions with and without a steep, mid-crustal, ramp along the MHT is shown in Supplementary Fig. 7 for the two main interferogram phase data sets. The comparison with the seismological moment tensors is shown in Supplementary Table 2. The modelled 3D displacement field is given in Supplementary Fig. 11, and shows a peak of 130 cm of uplift just north of Kathmandu, and over 65 cm of subsidence further north. Most horizontal motion is in a south-southwest direction, with a modelled peak displacement of 170 cm. The individual three components of surface motion are shown in Supplementary Fig. 11.

The slip remains predominately below a depth of 11 km (Supplementary Fig. 4), over 50 km north from the MFT. Estimates of the expected ground shaking by the USGS for the mainshock based on a rupture area similar in extent to that found in this study indicate that the strongest shaking as measured on the modified Mercalli intensity scale (VII & VIII) is expected only north of the MFT. This is in contrast to that estimated for the 1833 earthquake[51], which sees much stronger shaking along and to the south of the MFT (Supplementary Fig. 1), suggesting shallower rupture given similar estimated magnitudes.

Aftershock 12 May. We also calculate the distribution of slip from the largest aftershock of the Gorkha earthquake from 12 May, based on the InSAR data downsampled as described before for the mainshock (Supplementary Fig. 10). The comparison of the model with the full resolution InSAR data is shown in Supplementary Fig. 12. We use the same fault geometry as found for the mainshock to calculate the magnitude of slip (Supplementary Fig. 4). The region of slip due to the aftershock lies at the lower northeast edge of the mainshock slip patch. Comparison with the seismological moment tensors is shown in Supplementary Table 2.

Code availability. The GAMMA software package used to compute the differential interferograms (InSAR) of ground motion can be accessed at http://www.gamma-rs.ch.

The COSI-Corr software package[41] used to determine the coseismic horizontal displacement field resulting from the Gorkha earthquake is available for free download from www.tectonics.caltech.edu/slip_history/spot_coseis/index.html.

The software code Classic Slip Inversion (CSI) used to model the fault and geometry will be released soon and is available on request from R.J. Calculation of the Green's functions in a layered elastic half space was achieved using the EDKS software[45].

References

39. Sansosti, E., Berardino, P., Manunta, M., Serafino, F. & Fornaro, G. Geometrical SAR Image Registration. *IEEE Trans. Geosci. Remote Sensing* **44,** 2861–2870 (2006).
40. Gonzalez, P. *FRINGE 2015 Workshop* (ESA, 2015).
41. Leprince, S., Barbot, S., Ayoub, F. & Avouac, J. Automatic and precise orthorectification, coregistration, and subpixel correlation of satellite images, application to ground deformation measurements. *IEEE Trans. Geosci. Remote Sensing* **45,** 1529–1558 (2007).
42. Leprince, S., Ayoub, F., Klinger, Y. & Avouac, J.-P. *Geoscience and Remote Sensing Symposium, 2007* 1943–1946 (IEEE, 2007).
43. Leprince, S., Muse, P. & Avouac, J. In-flight CCD distortion calibration for pushbroom satellites based on subpixel correlation. *IEEE Trans. Geosci. Remote Sensing* **46,** 2675–2683 (2008).
44. Ayoub, F., Leprince, S. & Avouac, J.-P. Co-registration and correlation of aerial photographs for ground deformation measurements. *ISPRS J. Photogramm. Remote Sensing* **64,** 551–560 (2009).
45. Zhu, L. & Rivera, L. A. A note on the dynamic and static displacements from a point source in multilayered media. *Geophys. J. Int.* **148,** 619–627 (2002).
46. Simons, M., Fialko, Y. & Rivera, L. Coseismic deformation from the 1999 M_w 7.1 Hector Mine, California, Earthquake as inferred from InSAR and GPS observations. *Bull. Seismol. Soc. Am.* **92,** 1390–1402 (2002).
47. Sudhaus, H. & Jónsson, S. Improved source modelling through combined use of InSAR and GPS under consideration of correlated data errors: application to the June 2000 Kleifarvatn earthquake, Iceland. *Geophys. J. Int.* **176,** 389–404 (2009).

48. Jolivet, R. *et al.* The 2013 M_w 7.7 Balochistan Earthquake: seismic potential of an accretionary wedge. *Bull. Seismol. Soc. Am.* **104,** 1020–1030 (2014).
49. Ortega Culaciati, F. H. *Aseismic Deformation in Subduction Megathrusts: Central Andes and North–East Japan* PhD thesis, California Institute of Technology (2013).
50. Patil, A., Huard, D. & Fonnesbeck, C. J. PyMC: Bayesian stochastic modelling in Python. *J. Stat. Softw.* **35,** 1–81 (2010).
51. Bilham, R., Bodin, P. & Jackson, M. Entertaining a great earthquake in Western Nepal: historic inactivity and geodetic tests for the present state of strain. *J. Nepal Geol. Soc.* **11,** 73–78 (1995).